International Journal of Heat and Mass Transfer 195 (2022) 123057

Contents lists available at ScienceDirect

International Journal of Heat and Mass Transfer

journal homepage: www.elsevier.com/locate/hmt

Convective heat transfer in pine forest litter beds

Eric V. Mueller[a,d,*], Michael R. Gallagher[b], Nicholas Skowronski[c], Rory M. Hadden[d]

[a] National Institute of Standards and Technology (NIST), Gaithersburg, MD 20899, USA
[b] USDA Forest Service, Northern Research Station, PO Box 251, New Lisbon, NJ 08064, USA
[c] USDA Forest Service, Northern Research Station, 180 Canfield St., Morgantown, WV 26505, USA
[d] School of Engineering, The University of Edinburgh, Edinburgh, EH9 3FB, UK

ARTICLE INFO

Article history:
Received 3 March 2022
Revised 1 May 2022
Accepted 19 May 2022
Available online 5 July 2022

Keywords:
Multiphase flow
Porous media
Convective heat transfer
CFD modeling

ABSTRACT

To properly parameterize physics-based models of wildland fire behavior, it is necessary to understand the magnitude of convective heat transfer in various scenarios. In order to do so, we isolated the convective heating process in an idealized wildland fuel: pine needle litter layers. A heated wind tunnel was used to obtain a Reynolds number dependent correlation for the Nusselt number for: (1) a single representative fuel element, and (2) the bulk porous medium - both exposed to sudden pulses of high temperature air. The former was obtained through resistive thermometry and the latter through optimization of a 1-dimensional advection-diffusion model, trained by gas-phase measurements. It was determined that the Nusselt number for a single fuel element, when oriented perpendicular to the flow, did not significantly deviate from that of a single isolated cylinder. However, the correlation for the bulk medium showed a Nusselt number roughly 11% to 25% less than that of a single cylinder, over the range studied. This was attributed to the complex orientation of individual elements within the bed and has implications for modeling ignition and flame spread in porous fuels.

1. Introduction

Proper quantification of the heat transfer mechanisms for solid vegetative fuels is a key component of any physics-based evaluation of wildland fire dynamics. These mechanisms will drive both the potential for ignition of fuel and the subsequent burning rate. Convective heat transfer is one such mechanism, and historically it has not been well quantified in wildland fire research. The magnitude of convective heat transfer to fuel elements is difficult to measure in realistic conditions. It depends on the thermal and momentum boundary layers [1], and thus the properties of individual fuel elements and on highly localized flow conditions. This is in contrast to thermal radiation, which is comparatively easy to measure experimentally.

Despite the difficulties in directly quantifying convective heat exchanges, the importance of this mechanism has been identified by a number of researchers over the past 50 years. In a laboratory study, Rothermel and Anderson [2] compared fuel-particle and gas-phase temperatures, and identified the potential for convective preheating at least 2 m ahead of wind-driven fires in beds of pine needles. Anderson et al. [3] measured flow velocity and gas-temperature ahead of wind-driven laboratory fires in pine needle and excelsior fuel beds, as a function of free-stream wind and fuel structure. They demonstrated the potential for convective preheating, depending on the conditions of a particular test. In another set of laboratory experiments, in this case with fuel beds of manufactured cardboard tines, Finney et al. [4] measured gas-phase temperatures and determined that intermittent pulses of convective heating ahead of the main flame front were key in wind-driven fire spread.

Cooling by convection may also be important in certain scenarios. Bouyancy-generated indrafts downwind of flame fronts has been observed in laboratory and field settings [3,5], and these may serve to offset the effects of long-range radiative heating. In an effort to model fire spread at laboratory scale in still air, Albini [6] found that the inclusion of a convective cooling term was important for this reason. Understanding the role of heating versus cooling may also be helpful when exploring the difference in the functional dependence of spread rate on wind speed for head fire (concurrent flow) and backing fire (opposed flow) [7].

Therefore, the ability to quantify and then model the role of convective heat transfer is key when building a model of wildland fire spread. This is particularly true in the case of detailed physics-based Computational Fluid Dynamics (CFD) models. These models attempt to capture a range of potential fire dynamics by avoiding certain a-priori assumptions (e.g. assuming the dominance of

* Corresponding author. National Institute of Standards and Technology (NIST), Gaithersburg, MD 20899, USA.

E-mail address: eric.mueller@nist.gov (E.V. Mueller).

https://doi.org/10.1016/j.ijheatmasstransfer.2022.123057
0017-9310/Published by Elsevier Ltd.

Nomenclature

Latin letters

A_p	particle surface area (m^2)
Cr	Courant number (−)
c_p	specific heat capacity (J kg^{-1} K^{-1})
d	particle diameter (m)
Fo	Fourier number (−)
h_c	convective coefficient (W m^{-2} K^{-1})
k	thermal conductivity (W m^{-1} K^{-1})
L	bed length (m)
Nu	Nusselt number (−)
Pr	Prandtl number (−)
Re	Reynolds number (−)
t	time (s)
$t*$	convective time scale (−)
T	temperature (C)
u	velocity (ms^1)
V	volume (m^3), voltage (V)
x	distance (m)

Greek letters

α_Ω	temperature coefficient of resistance (K^{-1})
β	bed packing ratio (−)
ϵ	bed porosity (−)
ν	kinematic viscosity (ms^{-2})
ρ	density (kg m^{-3})
ρ_b	bed bulk density (kg m^{-3})
σ	particle surface-to-volume ratio (m^{-1})

Subscripts

Al	Aluminum
g	gas phase
n	pine needle
Ni	Nickel
p	particle
s	solid phase
0	initial value

a particular mode of heat transfer) [8], and they must therefore reproduce realistic values of convective fluxes.

A significant challenge in modeling convection is that the wildland fire problem encompasses a wide range of conditions. Flows can range from quiescent to as much as 60 m s^{-1} in crown fires [9], temperatures from tens of degrees in the surrounding environment to > 1000 °C in the combustion zone [10], and fuel structures from densely packed litter layers to sparse canopies. As a starting point, we focus here on forced convection conditions relevant to low-intensity fires in beds of dead pine needles. Such scenarios are relevant for fire management activities (prescribed burning) and have been the focus of many past experimental and numerical studies at different scales [e.g. 11, 12,13, 14] (this work is also a follow-on of a study on the fluid mechanics (i.e. bed drag) in the same type of fuels [15]). Management burns may make use of different fire types (i.e. head or backing fire), and as highlighted previously, the role of convection may vary under different conditions. Likewise, repeated burning in an area may change fuel structure [16]. Thus, improving our understanding of heat transfer in these fuels layers can improve our ability to plan fire management activities.

Given these conditions, we set out to directly quantify the convective heating process. To accomplish this, two sets of experiments were conducted in which pine needle fuel beds were exposed suddenly to convective heating. The first set of experiments involved the analysis of the thermal response of single element within a packed bed. This was done by using resistive thermometry on fuel element analogue: a nickel wire. The second set of experiments involved monitoring of gas-phase temperatures within the fuel bed, in order to infer a bed-average coefficient of convective heating. This was done by creating a simple 1-dimensional advection-diffusion model and optimizing the convective coefficient to best match the experimental data. The results of this optimization are then able to be implemented in other more complex models, and in this case they were tested in a detailed CFD fire behavior model, the Fire Dynamics Simulator.

2. Background theory

2.1. Forced convective heating of particles

A typical approach in detailed models of wildland fire behavior is to consider the solid fuel as a collection of highly dispersed thermally-thin particles which occur at an unresolved (subgrid) scale in the gas-phase domain [17,18]. Thus the convective heat transfer within this multiphase medium can be represented by the summation of individual particle contributions within a control volume:

$$q_c''' = \frac{1}{V}\sum_n A_p h_c (T_g - T_s) = \sigma\beta h_c (T_g - T_s), \quad (1)$$

where A_p is the surface area of a single particle, σ is the surface-to-volume ratio of a single particle, and β is the packing ratio (or solid volume fraction). The convective coefficient, h_c, may be determined as a function of the non-dimensional Nusselt number, Nu [1]:

$$h_c = \frac{k_g \sigma Nu}{4}. \quad (2)$$

In this case, we assume particles to be roughly cylindrical (such as pine needles, branches, etc.) so the characteristic length is taken as the diameter ($d = 4/\sigma$). Nusselt number relationships for cylindrical particles in forced convection generally take the form of a power-law:

$$Nu = C Re_p^m Pr^n, \quad (3)$$

where $Re_p = 4u/\sigma\nu$ is the particle Reynolds number and Pr is the fluid Prandtl number. Generally, gas-phase properties in the preceding equations are evaluated at the so-called film temperature, $T_f = (T_g + T_s)/2$. Over the range of Reynolds numbers relevant in wildland fire scenarios, the following empirical relationship for single cylinders in cross flow [1] is often employed:

$$Nu = \begin{cases} 0.989 Re_p^{0.33} Pr^{1/3}, & 0.4 \le Re_p < 4 \\ 0.911 Re_p^{0.385} Pr^{1/3}, & 4 \le Re_p < 40 \\ 0.6839 Re_p^{0.466} Pr^{1/3}, & 40 \le Re_p \le 4000 \end{cases} \quad (4)$$

Under typical conditions, the Prandtl number can be taken as a constant, $Pr = 0.7$.

The use of Eq. (4) assumes that individual particles do not affect the convective heating of one another (e.g. no wake interactions), and that they are all oriented perpendicular to the flow. These assumptions do not necessarily apply to vegetative fuel layers. Nevertheless, they have been applied in a number of numerical studies for vegetation ranging from litter layers to trees and shrubs, as a better quantification is not available [e.g. 14, 19,20, 21].

2.2. Forced convective heating in packed beds

As with individual particles, quantification of convective heating in porous media has been carried out under a variety of flow conditions [e.g. 1, 22]. However, many of these studies involve bed porosities and Reynolds numbers outside the typical range encountered in wildland fuels. Likewise, assumptions related to particle

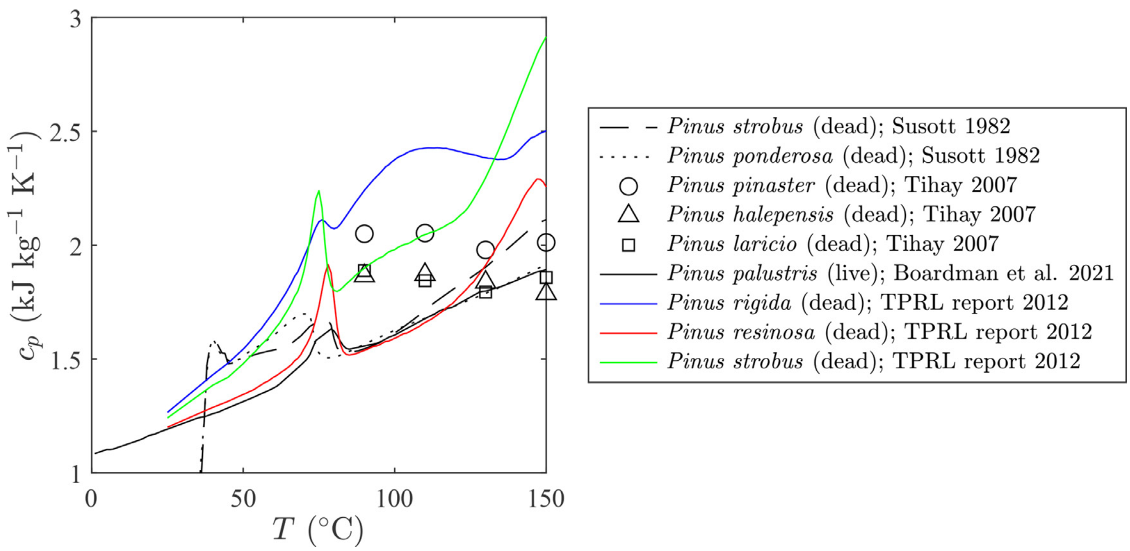

Fig. 1. Temperature dependence of specific heat capacity, c_p, for foliage of a variety of pine species, focused on pre-decomposition temperatures. Data extracted from Susott [26], Tihay [30], Boardman et al. [31] and an externally commissioned report [34].

sizes (and the potential for internal temperature gradients) or particle connectivity (and the potential for significant bed conduction) can impact the analysis of convective heating, and these must be considered with care when comparing between studies. Metal foams are one material which may begin to resemble beds of forest litter (high bed porosity with small diameter 'fibers'). A study carried out by Giani et al. [23] focused on forced convection for relatively low Reynolds numbers, similar to those considered relevant for fire spread in forest litter [15]. They identified an increase in the Nusselt number over the single-cylinder correlation. On the other hand, Mancin et al. [24] identified a comparative decrease in the Nusselt number for similar foams.

The discrepancies in these studies, and the fact that they are empirical in nature, demonstrates the necessity to determine a suitable correlation for the bed of interest in this case. At present, very little research has been carried out specifically on vegetative fuels for wildland fire applications. An initial investigation of pine needle beds was made by Mendes-Lopes et al. [25], which suggested a significant over-prediction of the Nusselt number when using the single-cylinder correlation. However, this work was limited in scope, and it is necessary to explore the problem further.

2.3. Material response to heating

Considered in isolation, the convective coefficient is not particularly useful for modeling wildland fires. In order to understand the potential for ignition (and thus flame spread) the overall thermal response of the fuel to a particular heating scenario must be understood. For wildland fuels, this will include the effect of solid-phase reactions. These may be endothermic (drying and pyrolysis) or exothermic (char oxidation). However, at present we seek to isolate the behavior from these complexities and thus focus on dry fuels at temperatures below 200 °C, and thus the onset of pyrolysis [26–28] and char oxidation [29].

If the particles are thermally thin, the remaining parameters of interest are the material density, ρ_s, and the specific heat capacity, c_{p_s}. Assuming no thermal decomposition and no expansion or contraction of individual needles, the density should remain constant. The specific heat, on the other hand, is often reported as a function of temperature for cellulosic materials.

Perhaps the most well-known study on the specific heat of material relevant to the wildland fire problem is that of Susott [26].

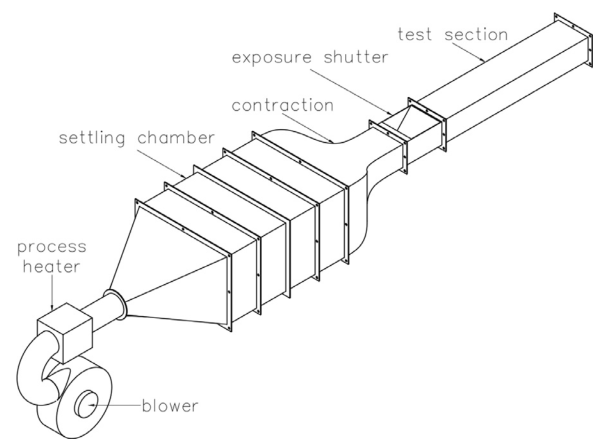

Fig. 2. WEIRD design.

He provided an estimate of the specific heat at low temperatures for both woody material and foliage of several pine species. In a more recent study, Tihay [30] reported specific heat values for the dead foliage of three pine species at temperatures between 80 °C and 200 °C. Boardman et al. [31] also evaluated the specific heat of a range of foliage, in this case focused on live material. A summary of the available data specifically for pine needles is given in Fig. 1.

These data have considerable scatter, particularly at higher temperatures. Unfortunately, only one of the species was tested in multiple studies (*Pinus strobus*), and the difference between the two results encompasses nearly the entire range of scatter for the available data. Therefore, it is difficult to attribute the scatter to differences in species chemistry, rather than difficulties in obtaining and processing the data. A more robust characterization of the specific heat capacity remains an outstanding challenge, as few researchers have focused on this parameter. However, Fig. 1 provides a starting place for evaluating the response of pine needles to convective heating in this study.

3. Experimental methods

Convective heating experiments were carried out in a stainless steel wind tunnel designed to produce flows characteristic of conditions encountered in wildland fires, known as the WEIRD (Wild-

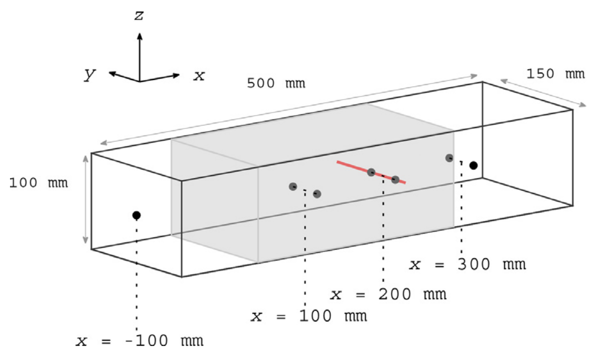

Fig. 3. Wind tunnel test section configuration. The shaded region shows the volume of the packed fuel bed. Black dots indicate thermocouple locations, and the red line indicates the resistive wire measurement location (note this wire was only included in the relevant subset of experiments). (For interpretation of the references to color in this figure legend, the reader is referred to the web version of this article.)

Fig. 4. (a) Example of *Pinus rigida* needles, which are grouped with three individual needles on one fascicle. (b) Example of fuel bed packing before test section lid is placed.

fire Exposure and Ignition Response Device). Using a blower and process heater, high temperature air flows can be generated. A divergent section, a settling chamber with a honeycomb straightener, and a contraction section are all used to help condition the flow. An enclosed test section, with dimensions of 750 mm × 150 mm × 100 mm, was attached to the contraction outlet and can be isolated from the flow via an exposure shutter. The walls of the test section were lined with ceramic paper insulation to minimize heat losses. The full system in shown in Fig. 2.

Within the test section, porous fuel beds were comprised of dead pine needles of the species *Pinus rigida* (common name: pitch pine). These have been the focus of a number of previous studies on the mechanisms of fire spread in forest litter [e.g. 32, 33], and the particle properties have been extensively characterized [34]. The surface-to-volume ratio for single needle was taken to be $\sigma = 4661$ m^{-1} (giving an equivalent cylindrical diameter of $d = 4/\sigma = 0.86$ mm), and the dry material density was $\rho_s = 615 \mathrm{kgkgm}^{-3}$. Pine needles were oven-dried for at least 24 h before being tested in order to minimize the effect of moisture mass and the latent heat of vaporization on the thermal response of the fuel.

The fuel beds tested were 250 mm in length and filled the entire area of the test section, shown in Fig. 3. The bulk density (and therefore packing ratio or porosity) was varied depending on the specific test, as described in the following sections. Fig. 4 shows the typical appearance of both individual particles and the packed beds.

In a given test, the fuel beds were instantaneously exposed to a high-temperature air stream (110 °C to 120 °C) at seven velocities, covering a range of nominally 0.5 ms^{-1} to 2.0 ms^{-1}. The test section was initially detached from the rest of the wind tunnel, with the air diverted upwards by a shutter. When a quasi-steady temperature was attained at the desired velocity, the test section was attached and the data logging was started. After a period of recording initial values, the shutter was opened and the sample exposed for a duration of 50 s. After each experiment, the test section was removed and cooled to ambient temperature before repeating at the next velocity set-point.

Gas-phase temperatures were measured with very fine gauge (0.08 mm) *K*-type thermocouples. These were chosen in order to minimize response times and radiative effects and characterize gas-phase temperature more accurately. An absolute standard uncertainty of ±2 °C was estimated for these measurements. Exposure velocity was measured with an *S*-type pitot tube connected to a digital differential pressure transducer. This was positioned between the exposure shutter and the sample at the centerline of the tunnel, and was temperature-compensated with an adjacent thermocouple. By applying the manufacturer-specified accuracy for the pressure and temperature measurements to the propagation of uncertainty law [35], a relative combined standard uncertainty of ±3% was estimated for the velocity measurements. All measurements were sampled at 10 Hz.

Thermocouples were located upstream of the fuel bed (as a control measurement for the exposure conditions), at four locations within the fuel bed, and at two locations downstream of fuel bed (see Fig. 3). Measurements at equivalent streamwise locations but offset by 4 cm in the spanwise direction were used to reduce experimental uncertainty resulting from local fuel bed structure, assuming a 1-dimensional response at macroscopic scale.

Intra-bed thermocouples were initially protected by a steel sheath entering from the base of the test section, and the fuel bed was packed around them. The sheath was then lowered to expose the bare tip of the thermocouple. This was done in order to create a small air pocket around the thermocouple and avoid direct contact with pine needles, which could skew the measurement from the gas-phase value.

3.1. Resistive analogue experiments

In order to directly measure the response of an individual solid-phase particle, a nickel wire (Ni 200 alloy) was positioned at the mid-height of the tunnel ($z = 50$ mm), as shown in Fig. 3. Its temperature was monitored by measuring the change in resistance during exposure. The wire was placed within a pine needle bed with a bulk density, ρ_b, of 40 kg m^{-3}, in order to identify any influence of the surrounding bed on the convective heating. Three repeats of this test were conducted.

This approach was adopted because measuring the temperature of an actual pine needle is very difficult. Issues arise in creating a good thermal contact with a thermocouple and in avoiding modification of the thermal response of the needle due to the presence of the thermocouple itself. Thermal imaging techniques avoid these issues but have limited use for measuring temperature deep within a packed bed.

The nickel wire acts as a pine needle analogue, and its temperature can be measured directly through resistive thermometry. It has different thermophysical properties from a pine needle, so the absolute temperature response will differ, but the behavior can be understood in non-dimensional terms (*Re* and *Nu*), which should hold for other similar objects, such as the pine needles. A key assumption is that contact conduction between elements in the bed

Table 1
Material properties relevant to the experimental and numerical analyses.

Property	Vaule	Units	Ref.
$c_{p_{Al}}$	$882 + 0.586T$	J kg^{-1} K^{-1}	[38] [a]
c_{p_g}	1000	J kg^{-1} K^{-1}	[1]
$c_{p_{Ni}}$	$420 + 0.523T$	J kg^{-1} K^{-1}	[1][a]
c_{p_n}	$1100 + 8T$	J kg^{-1} K^{-1}	Fig. 1
k_g	0.03	W m^{-1} K^{-1}	[1]
α_Ω	0.0047	K^{-1}	[b]
ρ_{Al}	2700	kg m^{-3}	[1]
ρ_g	1.0	kg m^{-3}	[1]
ρ_{Ni}	8900	kg m^{-3}	[1]
ρ_n	615	kg m^{-3}	[34]
σ_{Al}	5000	m^{-1}	
σ_{Ni}	4000	m^{-1}	
σ_n	4661	m^{-1}	[15,34]

[a] Fit to reported tabular values over relevant temperature range.
[b] Similar to reported values, but calibrated here to reproduce idealized behavior of a cylinder in crossflow.

is negligable. This is a common assumption applied to similar fuels, owing to the high porosity (>90%, here).

The the nickel 'needle' was 110 mm long and 1 mm in diameter. Its thermal response can be approximated using a lumped capacitance approach [1], which yields the following equation for the Nusselt number:

$$Nu = \frac{4\rho_s c_{p_s}}{\sigma^2 k_g}\frac{dT_s}{dt}(T_g - T_s)^{-1}. \tag{5}$$

This approach ignores radiative effects, which should be small as the emissivity of nickel at low temperatures is $\epsilon < 0.1$ [36]. Density and specific heat were assumed equivalent to that of pure nickle (see Table 1). The gas-phase temperature was taken as the average of two measurements: one at the center of the wire and the other at an endpoint, as shown Fig. 3.

The resistivity of the wire increases with temperature according to a temperature coefficient of resistance, α_Ω. A current of nominally 700 mA was supplied to the wire with a constant current source, and the voltage drop, V, over the wire was measured with an Analog-to-Digital Converter (ADC) using 4-point resistance measurement (in order to remove any effect of voltage drop over the sensing leads) [37]. The wire temperature can then be calculated as:

$$T_s = \left(\frac{V}{V_0} - 1\right){\alpha_\Omega}^{-1} + T_{s_0}. \tag{6}$$

The initial values, V_0 and T_{s_0}, were determined for each test from the first 20 s of measurements prior to opening the exposure shutter (assuming the wire starts in thermal equilibrium with the gas-phase).

Values of α_Ω for Ni 200 can be found in material datasheets. However, in this case the system was calibrated in the absence of a surrounding fuel bed, thus assuming the cylinder-in-crossflow model for convection can be applied (Eq. (4)). Matching the expected response to the observed response provided a calibrated value of $\alpha_\Omega = 0.0047$ K^{-1}.

Based on manufacturer specifications for the ADC, an error on voltage measurements of ±40 μV was assumed. Using the propagation of uncertainty, including the estimated uncertainty for gas-phase temperature, an average absolute standard uncertainty for solid-phase temperatures of ±4 °C was estimated. The temperature derivative required in Eq. (5) was computed with a central difference scheme, and a 50-point moving average was subsequently applied to reduce the effect of signal noise.

3.2. Optimization experiments

Another series of experiments was conducted to characterize the response of the entire bed, rather than a single element. In this case, all of the gas-phase measurement points shown in Fig. 3 were used to provide training data for a model optimization approach. A simple 1-D model of the system response was formulated, as described in Section 4, and the convective heating (Nusselt number) of the fuel beds could be inferred by fitting the numerical results to the experimental data.

Bed bulk densities of 20 kg m^{-3}, 40 kg m^{-3}, and 60 kg m^{-3} were tested. The values were determined by placing known masses of dry pine needles into the pre-defined test section volume. These correspond to bed porosities, ϵ, of 0.967, 0.935, and 0.902, respectively ($\epsilon = 1 - \beta = 1 - \rho_b/\rho_s$). For the lowest bulk density case, a very fine steel wire mesh was placed just below the mid-height of the test section in order to support fuel structure and ensure equal distribution along height. The mesh was positioned in such a way as to avoid interference with any intra-bed measurements. Three repeats (involving a full re-packing of the bed) were tested for each combination of velocity and bulk density. However, the resistive wire experiments (described in Section 3.1) provided an additional two repeats for the 40 kg m^{-3} condition, and these were included in the optimization analysis. In a related study on the flow through these types of fuel beds, it was determined that random variability introduced by manually packing the bed did not dominate over the effect of varying overall bulk density [15].

In addition to the pine needle tests, three tests were carried out with surrogate beds of metal wire. The aim was to reduce the complexity of the material heating response (as discussed in Section 2.3) as well as to provide a well-defined cylindrical particle geometry when compared to the more complex shape of pine needles. Aluminum wire was chosen, as it can be considered inert in the relevant temperature range (no drying, pyrolysis, or oxidation reactions) and has a specific heat which is easier to characterize. MIG wire with a diameter of 0.8 mm and cut to lengths of nominally 10 cm was used. For the purposes of this study, the wire is considered to be pure aluminum and the material properties are shown in Table 1.

The wires were packed in a random orientation following the same approach as the pine needles. The rigidity of the wire did not allow for the easy creation of beds with varying porosity while maintaining global homogeneity. Therefore, only one bulk density was tested, and through trial-and-error, a value of 138 kg m^{-3} was chosen. This density resulted in a bed porosity of 0.949. This is equivalent to a 31 kg m^{-3} bed of *Pinus rigida*, which is within the range tested and allows for meaningful comparison.

4. Numerical methods

4.1. 1-D model

In order to reproduce the gas- and solid-phase responses in the WEIRD, a simple 1-D advection-diffusion model of the gas-phase is proposed:

$$\epsilon\rho_g c_{p_g}\frac{\partial T_g}{\partial t} + u\rho_g c_{p_g}\frac{\partial T_g}{\partial x} = \epsilon k_g \frac{\partial^2 T_g}{\partial x^2} + \sigma\beta h_c(T_s - T_g), \tag{7}$$

where ϵ is the porosity (volume fraction of gas). The second term on the RHS, the convective heat transfer between phases, is obtain by modeling the solid-phase temperature as:

$$\rho_b c_{p_s}\frac{\partial T_s}{\partial t} = \sigma\beta h_c(T_g - T_s), \tag{8}$$

where ρ_b is the bulk density (equivalent to the packing ratio multiplied by the material density, $\beta\rho_s$).

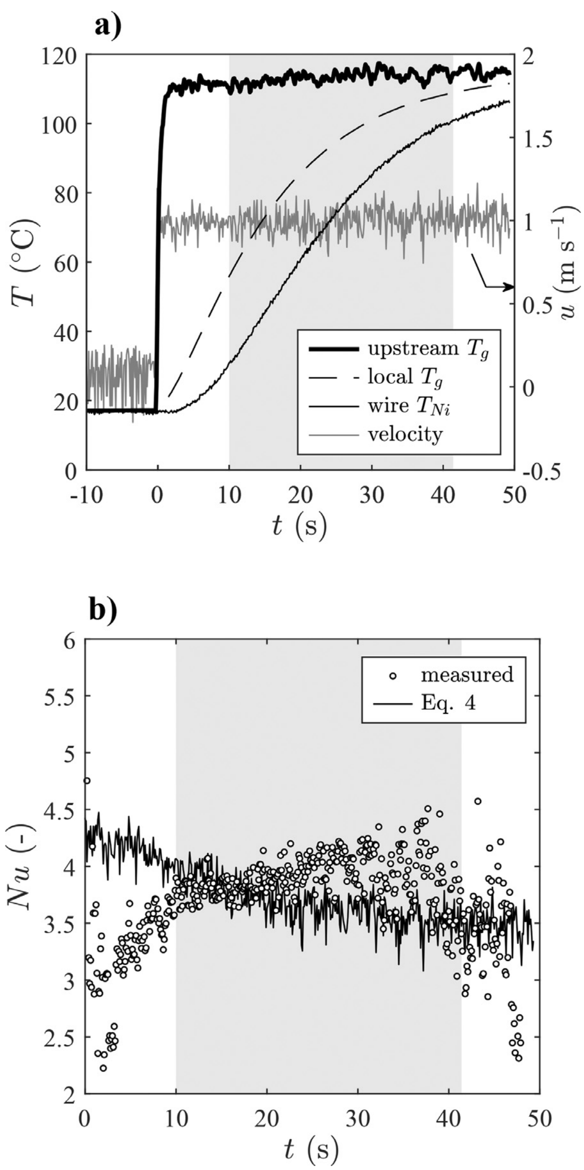

Fig. 5. Example resistive wire results for one test at an upstream flow of 1 ms^{-1}. (a) The gas and solid phase temperature responses. (b) The measured Nusselt number (circles) compared with that which would be obtained from Eq. (4) for the same exposure conditions (solid line). In both plots, the shaded area represents the region of interest used to generate statistical information.

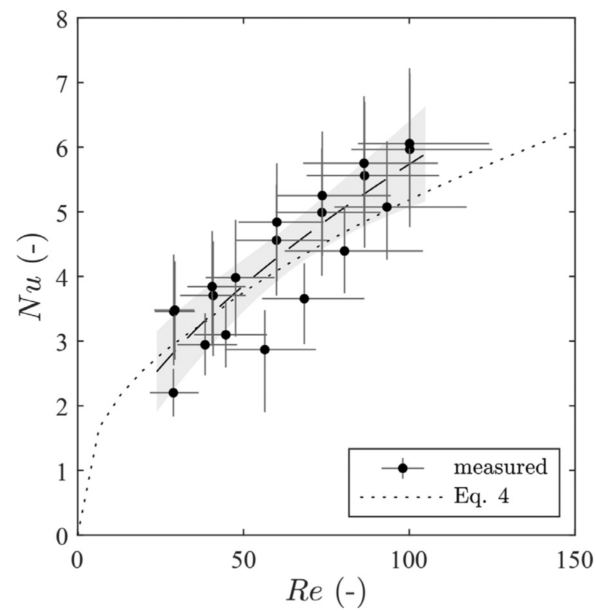

Fig. 6. Nusselt number computed for the nickel wire using Eq. (5) for all experimental cases. Points represent averages of *Re* and *Nu* over the window of interest, and error bars represent the combined measurement uncertainty for a given test. The dashed line represents a fit of the average values to a function of the form in Eq. (3), and the shaded region covers the 95% prediction interval for this fit. The dotted line shows Eq. (4) for comparison.

This coupled model involves a number of key simplifying assumptions. The gas phase is treated as a single, incompressible species, with constant properties representative of dry air (see Table 1). The use of a constant density is necessitated in order to conserve mass, due to the incompressible assumption. The use of a constant thermal conductivity is considered acceptable as the ratio of advective transport to diffusive transport, or the Peclet number ($Pe = Lu\rho c_p/k$), was in the range of 4000 to 20,000. Thus, a simplified treatment of gas-phase thermal conductivity should not significantly impact the results. These constants also ignore any effects of moisture, however, the ambient laboratory air had a water vapor mass fraction of $<$1.0%, and the impact on effective properties is deemed negligible here.

The velocity is assumed constant along distance. Changes in velocity at the inlet are experienced instantaneously at any downstream location:

$$u(x,t) = u(0,t) = f(t), \tag{9}$$

with the function $f(t)$ obtained from the experimental data. This was considered acceptable as the velocity essentially underwent a step change, from zero to constant exposure flow, which traversed the fuel bed in $<$1 s

For simplicity, solid-phase conduction is neglected. In previous models of pine needles beds it was assumed that the high porosity of pine needle beds makes solid-phase conduction negligible [39]. In all cases studied here, the porosity exceeded 90%. This assumption is supported by the fact that the pine needles have relatively low thermal conductivity and thermal diffusivity [17], they are not necessarily oriented parallel to the thermal gradient, and do not necessarily make perfect thermal contact with one another. In past work, intra-bed radiation was included through an effective conduction coefficient, using the Rosseland approximation [39]. However, we also negelect thermal radiation in the model, as we assume intra-bed transfer will be low due to the relatively low temperatures ($<$150 °C) and the local similarity in temperature of neighboring fuel elements. Finally, taking into account the various reported values of specific heat capacity for pine needles (Fig. 1), an approximate function of $c_{p_p} = 1100 + 8T$ J kg^{-1} K^{-1} was chosen.

It is recognized that some of the above assumptions may be significant over-simplifications. However, the focus is on understanding how the selection of h_c impacts the solution, which can still be explored with this simple model. Further, simulations with a detailed CFD model, as described in Section 4.3, allow for increased complexity and the relative importance of these different assumptions can be considered.

The 1-D model was discretized using the Crank–Nicolson method. This implicit method has the advantage of being unconditionally stable and second-order accurate, while still being possible to solve efficiently. The following initial and boundary conditions were used:

$$T_g(x,0) = T_s(x,0) = T_0, \tag{10}$$

$$T_g(0,t) = g(t), \tag{11}$$

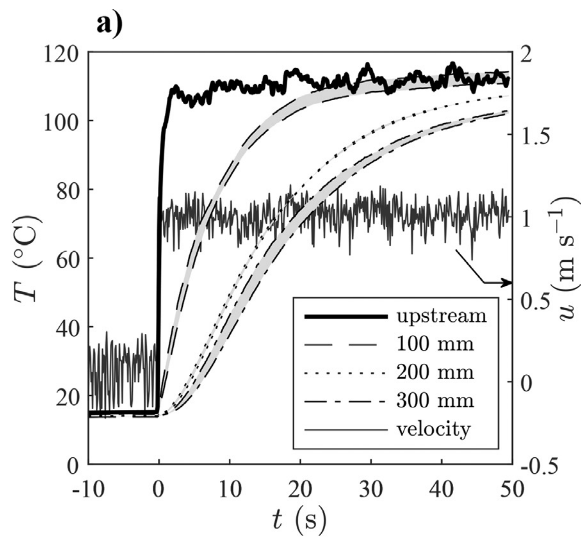

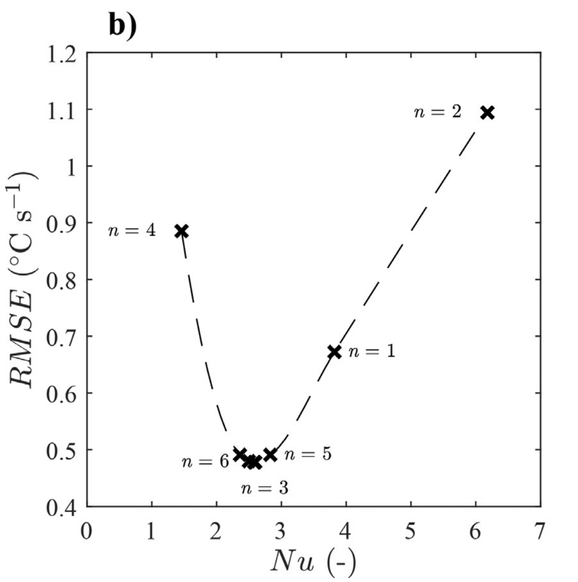

Fig. 7. Example of: (a) experimental data used for optimization, measured at the locations shown in Fig. 3, and (b) the convergence of the optimization scheme. The example case is had a flow of 1 ms^{-1} and a bulk density of 40 kg m^{-3}. Note that 13 guesses were required to converge on the minimum RMSE here, but those beyond the 6th guess are not labeled for the sake of readability.

$$\frac{\partial T_g(L,t)}{\partial x} = 0, \tag{12}$$

where $x = L$ is the downstream boundary. As with the velocity function, the time-history of the upwind boundary, $g(t)$, was obtained from experimental data for a given test. For further details of the solution procedure, please refer to Appendix A.

To reduce computational cost, while still resolving the transient phenomenon, a time step of $\Delta t = 0.1$ s was chosen. In order to fully resolve the spatial temperature gradient and to limit numerical oscillations introduced by the step changes entering and exiting the fuel bed and the over-simplification of momentum transport, a spatial increment of $\Delta x = 1$ mm was chosen. Sensitivity tests found that increasing spatial and temporal resolution further did not significantly change the overall results of the optimization.

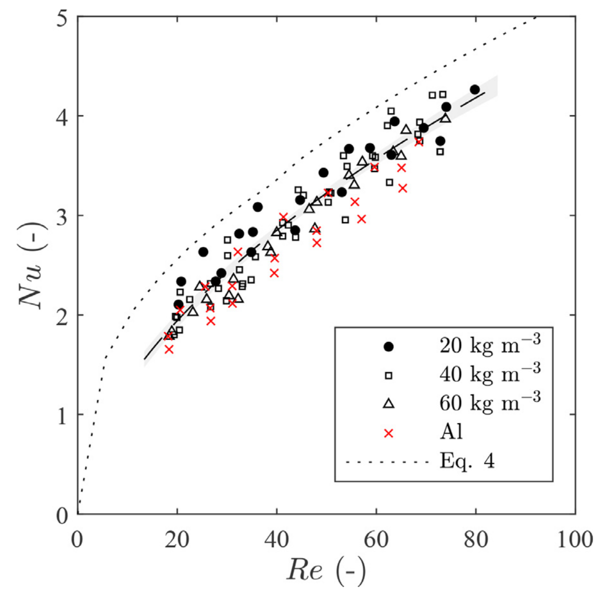

Fig. 8. Results of optimizing the Nusselt number, *Nu*, in the 1-D model for the various experimental cases. The best fit of the results is shown (dashed line), as well as the theory for a single cylinder in cross flow (dotted line).

4.2. Optimization scheme

The value of *Nu*, and therefore h_c in Eqs. (7) and (8), was determined through an iterative optimization technique. The chosen objective function was the Root Mean Squared Error (RMSE) between the 1-D model and the experimental observations of the time derivative of gas-phase temperature for a given test:

$$RMSE = \frac{1}{N}\sum_{i=1}^{N}\sqrt{(\dot{T}_{g,i} - \dot{T}^{*}_{g,i})^2} \tag{13}$$

The summation represents the average error over the $N = 6$ temperature measurements (four within the fuel bed and two downstream), starting from 3 s prior to exposure, until the end of each test. The objective function was minimized by selecting values of *Nu* using a hybrid of a golden-section search algorithm and parabolic interpolation.

Because the flow was nominally constant after exposure in a given test, *Nu* is considered a constant value when optimizing the simple model (as opposed to a function of *Re*, as in Eq. (4)). This reduces the number of free parameters in the optimization algorithm to one. Indeed, because each test represents a single flow condition, optimizing *Nu* as a function of *Re* for individual tests becomes an ill-posed problem. Instead, we use the constant values of *Nu* for the various velocity conditions in order to propose a Reynolds-dependent function.

4.3. CFD model

In addition to the simple 1-D model, CFD simulations were carried out using the National Institute of Standards and Technology (NIST) Fire Dynamics Simulator (FDS), version 6.7.7 [40]. This CFD model employs a large eddy simulation approach for solving a low-Mach number formulation of the Navier-Stokes equations. It is designed for simulating flows for a range of fire-related phenomena, and therefore it includes additional numerical models for incorporating gas-phase combustion, thermal radiation, solid fuel degradation, particle transport, etc. Indeed, FDS was selected as it has been used recently to simulate flame spread in pine needle litter with similar properties to that studied here [e.g. 12, 14, 41], and it is important to understand how well convective exchanges are represented.

In the typical approach in FDS, subgrid-scale vegetation is incorporated with source and sink terms in the gas-phase conservation equations through a multiphase formulation. The solid phase is assumed to be highly disperse such that porosity effects are neglected in the gas-phase and flow is modeled with the superficial velocity [15]. Full details of the particular CFD framework are outside of the scope of this discussion; however, the specifics of the model formulation can be found in the technical documentation [42]. The key aspect here is that convection for a bed of cylindrical particles is modeled using Eq. (4), as discussed in Section 2.

Simulations of the experiments were conducted using both the default approach and the model obtained from optimization of the 1-D model. A 3-D domain was used, with the same dimensions indicated in Fig. 3. The upwind *yz*-boundary was set to match the reference temperature and velocity measured in a given experiment. The downwind *yz*-boundary was set to a zero pressure gradient (open outflow). Lateral boundaries were set to solid surfaces with a wall model to approximate the near-wall velocity gradient [42]. The solid walls were also set as adiabatic boundaries so that there were no lateral heat losses, in an idealized representation of the insulated test section walls in the experiment. The numerical grid resolution was $\Delta x = \Delta y = \Delta z = 5$ mm, and gas-phase temperatures were recorded at the same intra-bed and trailing edge locations shown in Fig. 3.

5. Results

5.1. Resistive analogue experiments

An example of data obtained from the experiments with the nickel wire ‘needle’ is given in Fig. 5. Upon opening the shutter, the upstream gas temperature rapidly jumps to the preset exposure value, as does the velocity. The local intra-bed gas temperature (average of the two thermocouples located at the nickel wire) responds more slowly due to the energy sink of the pine needles upstream of the measurement point. In this example case, it reaches the inlet value at the end of the 50s exposure. The measured wire temperature lags behind the corresponding gas-phase response, as expected. The temperature difference between phases and the derivative of the wire temperature are then used in Eq. (5) to calculate a Nusselt number.

This calculation of the Nusselt number has an inverse dependence on the difference between solid- and gas-phase temperature. The relative uncertainty is likewise sensitive to this value. Therefore, in order to restrict the analysis to regions where the difference is large, a region of interest for calculating the Nusselt number was selected by taking a window where the relative uncertainty was below 25%, as shown in the example in Fig. 5a. Samples within this time period were then used to obtain statistical information on the measured behavior in a given test.

An example comparison of the value of the Nusselt number obtained from the measurements and that which would be obtained from Eq. (4) is shown in Fig. 5b. In this case, the average values are 3.9 and 3.7 for the measured value and the single cylinder theory, respectively. In the theoretical case, the values decrease systematically over the interval, which can be traced back to a slightly decreasing Reynolds number as the film temperature increases (and the exposure velocity remains broadly constant). In the case of the direct measurement, there is a systematic increase. However, this is not the case across all experiments, and so it is unclear if this is due to some local changes in the flow or a feature of measurement uncertainty.

This analysis was repeated for all 20 experiments of this type[1], and the results are summarized in Fig. 6. The uncertainty in the values due to statistical variation is evaluated by obtaining the 2.5th and 97.5th percentiles of the observations. This can be combined with uncertainty estimates for instantaneous samples based on instrument accuracy (see Section 3) [35]. The error bars in Fig. 6 represent an effective combined uncertainty, which has an average relative value of ±28% for the Reynolds number and ±20% for the Nusselt number.

A clear trend with increasing Reynolds number can be seen, and a fit of the experimental data overlaps the cylinder theory. While the best fit line has a slightly different slope, the 95% prediction interval suggests that with this current data we do not have the evidence to say that the measured response is different from that which would be predicted from Eq. (4).

5.2. Optimization of 1-D model

An example of a single gas-phase optimization experiment, as described in Section 3.2, is shown in Fig. 7a. As with the previously discussed example, the exposure conditions undergo a clear step-change. The gas-phase temperatures within and downstream of the fuel bed demonstrate the non-linear response both in time and space, hence the difficulty presented in directly calculating the convective heat exchange. The similarity between centerline and offset measurements at a given location suggests that the response is not strongly dominated by local bed structure. Some cases are less consistent than others, but the average temperature difference between the two measurements at a given streamwise location, after exposure, was 5 °C.

Each of the 83 experiments was run through the optimization scheme, which required around 10 to 15 iterations of the 1-D model to reach the cutoff criteria. These roughly 1000 simulations took around 60 seconds to complete, demonstrating one of the main advantages of using this simplified model, rather than optimizing with the CFD model. An example of the successive iterations for a single experimental case is shown in Fig. 7b. The scheme quickly converges to a clear singular minimum within the bounded region. Generally, guesses were within 10% of the optimal value by the 7th iteration.

Assuming the same functional form of the Nusselt number as that of Eq. (3) and that the Prandtl number is a constant of ∼0.7 raised to the power of $n = 1/3$, a fit of all optimization data points in Fig. 8 was carried out (ignoring tests with surrogate aluminum needles). In keeping with the formulation of FDS, the Reynolds number is calculated with the superficial velocity (ignoring the effect of porosity). The coefficients obtained were (with 95% confidence bounds) $C = 0.417 \pm 0.061$ and $m = 0.553 \pm 0.037$. Therefore, the resulting formula is:

$$Nu = 0.417 Re^{0.553} Pr^{1/3}. \tag{14}$$

Over the range of Reynolds numbers tested, this correlation is lower than Eq. (4) by 11% to 25%. Individual optimization results are scattered; however, they are bounded on the upper end by Eq. (4), with no values exceeding it, and they are up to 30% lower than that model. Despite the scatter, the narrow region of the 95% prediction interval suggests that additional tests would not substantially change the best fit line. There is no clear systematic effect of bulk density on the on the results, though the possibility for such a dependence may be masked by relatively narrow range of conditions (porosity between 0.902 and 0.967) and the scatter in the results. Further, replacing the pine needles with the aluminum surrogate yields the same overall behavior.

[1] 21 experiments were performed, but data were corrupt for one repeat of the 1 ms^{-1} exposure case

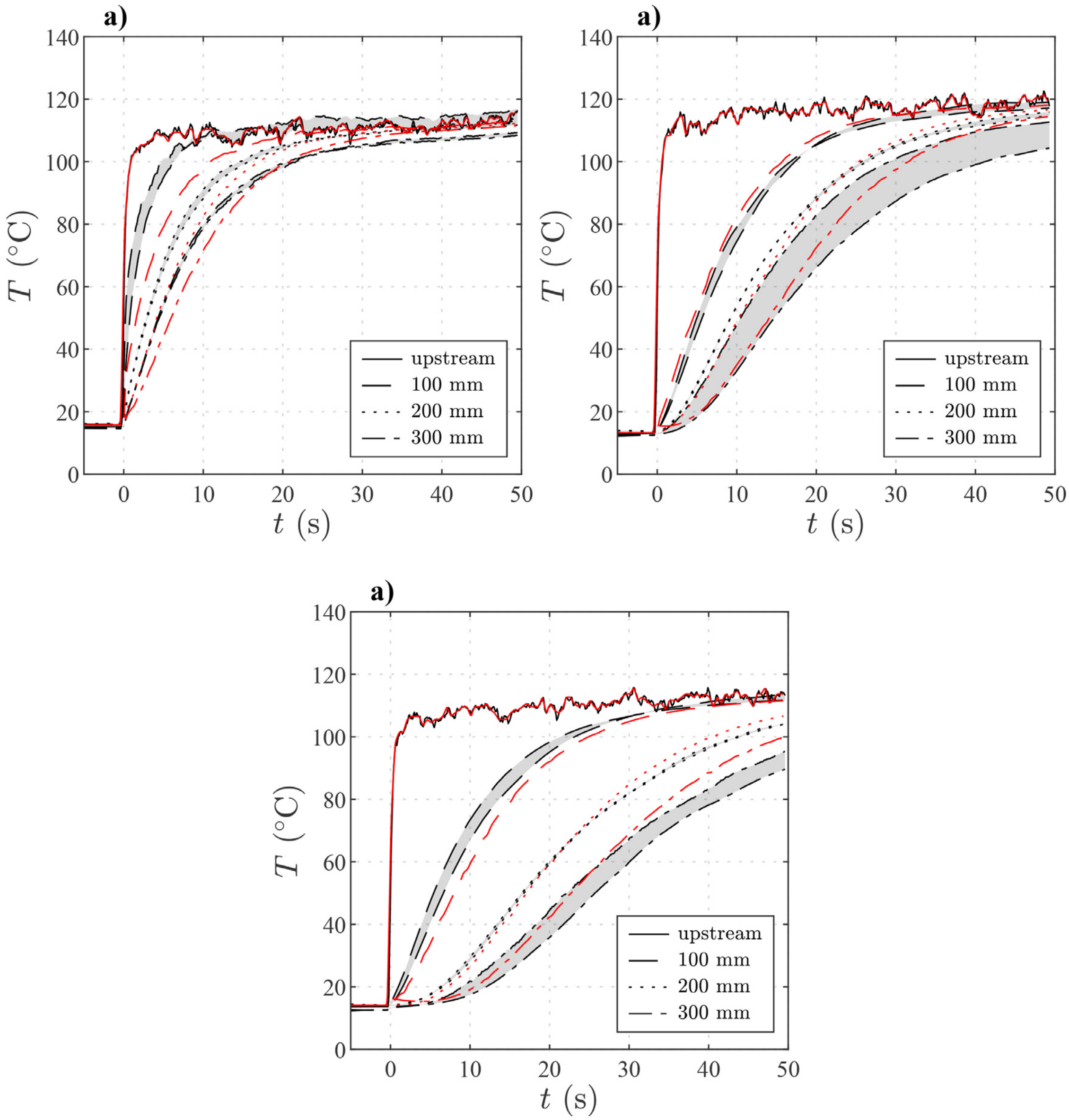

Fig. 9. Example results from FDS using the optimized convection model of Eq. (14). Results are shown for a flow of 1 ms^{-1} and a bulk density of (a) 20 kg m^{-3}, (b) 40 kg m^{-3} and (c) 60 kg m^{-3}. Black lines represent the experimental data and red lines represent the simulation results. The measurement locations correspond to those shown in Fig. 3. (For interpretation of the references to color in this figure legend, the reader is referred to the web version of this article.)

5.3. CFD simulations

Both the original model of Eq. (4) and the newly proposed model of Eq. (14) were implemented in the CFD model. Simulations were run using the initial and upwind boundary conditions measured in two repeats of each of the experimental conditions. Examples of the simulated gas-phase temperatures, obtained with Eq. (14), are shown in comparison to the experimental data in Fig. 9. Only the centerline ($y = 0$) simulation temperatures are shown as the adiabatic assumption for walls results in effectively no variation in the spanwise direction. The average difference between the two sample points at a given streamwise location in the CFD cases was <1 °C. The simulated gas-phase temperatures show the same overall response as the experiments and demonstrate that the correlation determined with the simple 1D model can be effectively applied in the more comprehensive CFD simulations. The measured behavior is reproduced over the range of bulk densities tested, though the fit appears worse for 20 kg m^{-3} case than the two higher bulk densities.

Beyond demonstrating that the CFD model is capable of replicating the experiments, the effect of implementing Eq. (14) in favor of Eq. (4) can also be quantified. Eq. (13) was used to compute the RMSE in gas-phase temperature gradients, the same as for the 1-D model. Fig. 10 shows the relative difference in error when the optimized convection model is used in favor of the default (where a negative value indicates a decrease in error). The optimized model reduced the RMSE in 39 of the 42 considered cases, with a maximum reduction of 36%. There was generally greater improvement for lower Reynolds numbers and for higher bulk density, with the

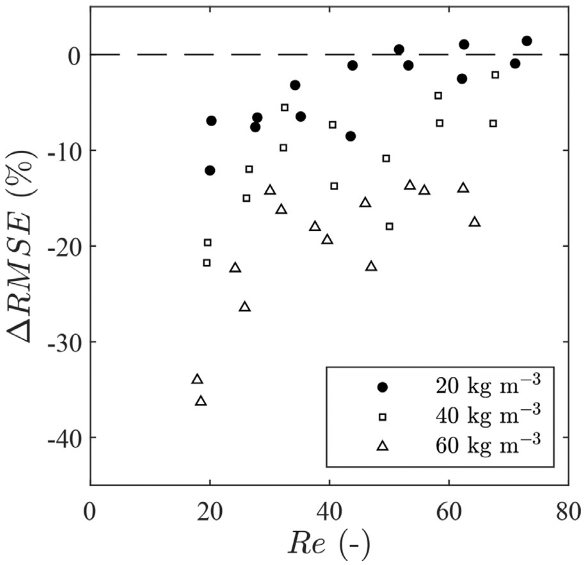

Fig. 10. Percent change in RMSE of temperature gradient (compared to the experimental data) when the optimized model of Eq. (14) is used in place of Eq. (4) with the CFD model, FDS.

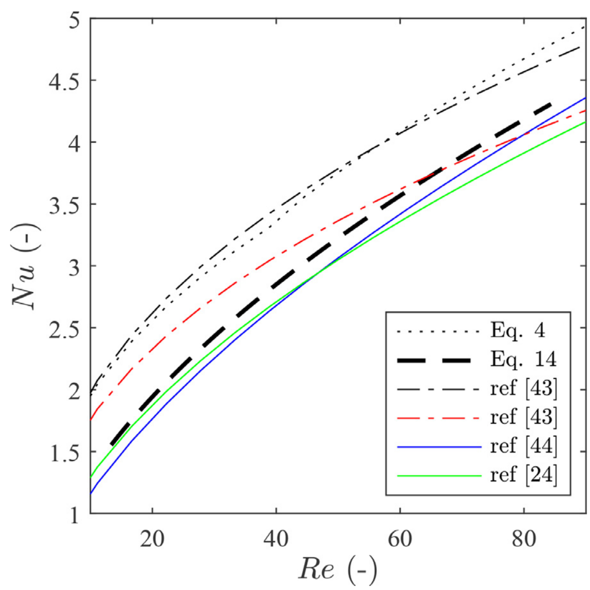

Fig. 11. Comparison of different possible models for convective heat transfer. The black dash-dot line is tube banks with staggered arrangement, while the red dash-dot line is for those with tubes aligned. The correlation from Mancin et al. [24] uses a porosity-dependent Reynolds number, so here we have scaled it by a mean value of 94% in order to compare directly. (For interpretation of the references to color in this figure legend, the reader is referred to the web version of this article.)

cases with slightly increased error occurring for the 20 kg m^{-3} fuel bed.

6. Discussion

The results of the nickel wire study suggest that a single element in the fuel bed may experience convective heating of similar magnitude to an isolated cylinder - assuming that single element is oriented perpendicular to the flow. Any change in needle orientation relative to the streamwise direction should modify the response from this idealized behavior, but this is difficult to investigate experimentally. As the orientation becomes more parallel to the flow, the heating will be affected by the surrounding temperature gradient (decreasing downstream due to the heat sink of surrounding elements) and even the potential for a solid-phase temperature gradient to establish along the length of the element.

The approach of optimizing the 1-D model aims to capture an average behavior of the fuel bed, rather than considering the detailed response of any one element. This is generally more appropriate for the formulation of the multiphase model. The findings indicate that the pine needle bed is overall less efficient at absorbing energy from the gas-phase in this scenario, when compared to an equivalent collection of parallel cylinders.

The individual results of this method are scattered, as mentioned in Section 5.2, with a mean difference of 5% from the proposed best fit. However, it is important to recall the that they do not represent a direct measurement of the Nusselt number, but rather a best-guess based on model fitting. The approach also relies on limited point measurements in a bed which will have some inherent variability in local structure. If it were possible to monitor the entire temperature field, experimental repeatability should improve significantly.

The results can be contextualized by considering other correlations for collections of cylinders or for packed beds. Some of these are shown in Fig. 11. Žukauskas [43] provided two correlations for tube banks over a similar range of Reynolds numbers (10 to 100): one where they are in staggered rows and one where they are aligned. The staggered arrangement is similar to a single cylinder, so the elements do not significantly influence one another at these Reynolds numbers, while the aligned arrangement does show some deviation and is a better match to the observed behavior at higher Reynolds numbers. As with the single cylinder, correlations for tube banks are determined with all elements perpendicular to the flow, so we cannot assume they would apply here. Nevertheless, an alternative correlation for tube banks was used to model pine needle beds by El Houssami et al. [44], with favorable results. This correlation is the similar to the optimized model determined here, over the range of conditions studied.

In terms of correlations specifically developed for porous media, Mancin et al. [24] studied metal foams with high porosities (>90%), small element diameter ($d < 1$ mm), and low Reynolds numbers (30 to 200). Their results are very similar to those determined here (see Fig. 11). Other correlations have been proposed for similar foams, but it is not the aim here to compare to every one. Rather this example demonstrates that behavior is not vastly different from other materials with similar global properties and random orientation of individual elements.

Finally, the fact that the bed of aluminum wires produced similar results indicates that the observed behavior was not dominated by thermo-physio-chemical behavior of the bed elements. While the protocol aimed to avoid the effects of dehydration (by pre-drying fuels) and pyrolysis (by limiting the exposure temperatures), the use of aluminum insures that these behaviors are absent. Further, the specific heat of aluminum has been well quantified, compared with pine needles. This suggests that the behavior is a direct result of the bed geometry, likely due to the varied particle orientation, as discussed previously. The similarity of the optimized Nusselt number for the wires also suggests that the behavior is not strongly dominated by the details of the surface characteristics or geometry individual elements. The effective diameter ($4/\sigma$) was roughly consistent between the two particle types, but the pine needles are not perfectly cylindrical and have different surface roughness. Nevertheless, it appears the response of the beds can be represented in the same way.

6.1. Implications for fire modeling

The results of Section 5.3 demonstrate a positive impact of using the optimized model in the CFD simulations with FDS. Interestingly, there does seem to be a greater improvement for the higher bulk density beds than for those with lower bulk density. This is despite the fact that there is no such trend in the Nusselt number which minimizes the overall error (see Fig. 8). Thus, tuning the Nusselt number is less able to account for model error in the lower bulk densities. This may be linked to the fact that lower bulk density beds have less of a dominating effect of convection, when compared to other potential influences (e.g., boundary effects, small non-uniformities in flow and temperature). It was also more more difficult to create globally homogenous fuel bed structure when dealing with such high porosities. More work would be needed to pinpoint the exact cause, however, and at this stage we can only suggest a single Nusselt number correlation, irrespective of bulk density.

It is also difficult to quantify how significant such a change in the Nusselt number would translate to fire modeling scenarios. Depending on the conditions, these can involve more complex flow dynamics, with rapid fluctuations [45] and heating rates potentially an order of magnitude greater [4,10]. As discussed in the introduction, the role of convection is not the same in all scenarios. Wind-driven fires will be influenced by convective heating [4], but radiation-dominated fires may also be affected by the magnitude of convective cooling [6]. Further complication may also be introduced in quantifying the convective heat transfer in cases where moisture vaporization and pyrolysis lead to a blowing effect that modifies the boundary layer [46].

Nevertheless, in a study of ignition and burning rate of pine needle beds with similar properties to those discussed here, El Houssami et al. [44] found that a modification of the convective coefficient to a model similar to that proposed here was necessary to model the observed behavior. This demonstrates that the quantity has the potential to play a significant role. More such studies are required in order to investigate model sensitivity to the magnitude of convective exchanges. However, this work provides an improved understanding of the range of possible values without relying on previous correlations which have not been directly demonstrated to hold true for vegetative fuel beds.

7. Conclusions

A better understanding of convective heat transfer in vegetative fuels is required to advance models of wildland fire behavior. To achieve this, we quantified the heating of pine needle litter beds under forced convection conditions, using a heated wind tunnel. The response of an individual element was measured directly, while the bed-average response was measured indirectly by monitoring the change in gas-phase temperatures and comparing to model results. These experiments led to the following observations:

- The heating response of an individual element, when oriented perpendicular to the flow, was not distinct from that which would be expected if it the surrounding bed were removed.
- A newly proposed model bed-average heating response was lower than that predicted for a single element perpendicular to the flow by 11% to 25%.
- Implementation of the new model in the CFD model (FDS), reduced the error between the model and experiments by up to 36%, when compared to the typical approach.

This work represents a first step, as it was not possible to cover the wide range of fuel structure and flow conditions which may be relevant in wildland fires. Further, we simplified the problem by focusing on heating in the absence of reactions, and the convective response of elements and beds may change as they pyrolyze and oxidize, and gaseous exchanges modify the boundary layer. Nevertheless, we can begin to understand the degree of uncertainty which may be present in relevant model parameters, and we hope that this new understanding and testing framework can continue to improve models of wildland fire behavior.

Declaration of Competing Interest

The authors declare that they have no known competing financial interests or personal relationships that could have appeared to influence the work reported in this paper.

CRediT authorship contribution statement

Eric V. Mueller: Conceptualization, Methodology, Investigation, Formal analysis, Visualization, Writing – original draft. **Michael R. Gallagher:** Funding acquisition, Resources, Writing – review & editing. **Nicholas Skowronski:** Funding acquisition, Project administration, Writing – review & editing. **Rory M. Hadden:** Project administration, Conceptualization, Supervision, Writing – review & editing.

Acknowledgments

The authors wish to thank Mark Partington and Jamie Graham for their instrumental role in constructing the WEIRD. We thank the Strategic Environmental Research and Development Program (SERDP) (grant RC-2641) and Forest Service International Joint Venture Agreement (No. 16-IJ-11242306137), for providing funding for this work.

Appendix A. 1-D numerical solution

For the numerical solution of the advection-diffusion equation, there are several key non-dimensional quantities, including the Courant number:

$$Cr = \frac{u\Delta t}{\epsilon \Delta x}, \tag{A.1}$$

and the Peclet number:

$$Pe = \frac{u\Delta x}{\epsilon \alpha}, \tag{A.2}$$

where $\alpha = k/\rho c_p$ and the ratio of the two is the Fourier number:

$$Fo = \frac{Cr}{Pe} = \frac{\alpha \Delta t}{\Delta x^2}. \tag{A.3}$$

Also important are the convective time scales:

$$t_g^* = \frac{\sigma \beta h_c \Delta t}{\epsilon \rho_g c_{p_g}}, \tag{A.4}$$

$$t_s^* = \frac{\sigma \beta h_c \Delta t}{\rho_b c_{p_s}}, \tag{A.5}$$

which have both gas-phase (t_g^*) and solid-phase (t_s^*) values.

With these definitions, we can use the Crank–Nicolson method to write Eq. (7) in a discrete form, at location i and time step n:

$$\begin{aligned}&[Cr - 2Fo]T_{g_{i+1}}^{n+1} + 4\left[1 + Fo + t_g^*/2\right]T_{g_i}^{n+1} \\ &- [Cr + 2Fo]T_{g_{i-1}}^{n+1} - \left[2t_g^*\right]T_{s_i}^{n+1} = [2Fo - Cr]T_{g_{i+1}}^{n} \\ &\qquad + 4\left[1 - Fo - t_g^*/2\right]T_{g_i}^{n} + [Cr + 2Fo]T_{g_{i-1}}^{n} + \left[2t_g^*\right]T_{s_i}^{n}.\end{aligned} \tag{A.6}$$

This formulation depends on the unknown solid phase temperature $T_{s_i}^{n+1}$, however, Eq. (8) can also be discretized following the Crank–Nicolson method:

$$T_{s_i}^{n+1} = \left[\frac{t_s^*}{2 + t_s^*}\right]\left(T_{g_i}^{n+1} + T_{g_i}^{n}\right) + \left[\frac{2 - t_s^*}{2 + t_s^*}\right]T_{s_i}^{n}. \tag{A.7}$$

These can be combined to give the following:

$$[Cr - 2Fo]T_{g_{i+1}}^{n+1} + 4\left[1 + Fo + \frac{t_g^*}{2 + t_s^*}\right]T_{g_i}^{n+1} - [Cr + 2Fo]T_{g_{i-1}}^{n+1} = [2Fo - Cr]T_{g_{i+1}}^{n} + 4\left[1 - Fo - \frac{t_g^*}{2 + t_s^*}\right]T_{g_i}^{n} + [Cr + 2Fo]T_{g_{i-1}}^{n} + \left[\frac{8t_g^*}{2 + t_s^*}\right]T_{s_i}^{n}. \quad (A.8)$$

Note that in regions of the domain where no solid phase is present $t_g^* = 0$, so no convective exchange occurs. When applying the boundary conditions specified in Eqs. (9)–(12) the linear system of equations:

$$A_i T_{g_{i+1}}^{n+1} + T_{g_i}^{n+1} B_i + T_{g_{i-1}}^{n+1} C_i = D_i \quad i = 1, \ldots, N \quad (A.9)$$

with the coefficients A_i, B_i, C_i, and D_i obtained from Eq. (A.8), can be written with a tridiagonal matrix which can be efficiently solved.

References

[1] F.P. Incropera, D.P. DeWitt, T.L. Bergman, A.S. Lavine, Fundamentals of Heat and Mass Transfer, Dekker Mechanical Engineering, vol. 6th, John Wiley & Sons, 2007, doi:10.1016/j.applthermaleng.2011.03.022.

[2] R.C. Rothermel, H.E. Anderson, Fire Spread Characteristics Determined in the Laboratory, Research Paper INT-30, USDA Forest Service, Intermountain Forest and Range Experiment Station, Ogden, Utah, 1966.

[3] W.R. Anderson, E.A. Catchpole, B.W. Butler, Convective heat transfer in fire spread through fine fuel beds, Int. J. Wildland Fire 19 (2010) 284–298, doi:10.1071/WF09021.

[4] M.A. Finney, J.D. Cohen, J.M. Forthofer, S.S. McAllister, M.J. Gollner, D.J. Gorham, K. Saito, N.K. Akafuah, B.A. Adam, J.D. English, Role of buoyant flame dynamics in wildfire spread, Proc. Natl. Acad. Sci. 112 (32) (2015) 9833–9838, doi:10.1073/pnas.1504498112.

[5] E.V. Mueller, N. Skowronski, J.C. Thomas, K. Clark, M.R. Gallagher, R. Hadden, W. Mell, A. Simeoni, Local measurements of wildland fire dynamics in a field-scale experiment, Combust. Flame 194 (2018) 452–463, doi:10.1016/j.combustflame.2018.05.028.

[6] F.A. Albini, Wildland fire spread by radiation-a model including fuel cooling by natural convection, Combust. Sci. Technol. 45 (1–2) (1986) 101–113, doi:10.1080/00102208608923844.

[7] G.M. Byram, Combustion of forest fuels, in: Forest Fire: Control and Use, McGraw-Hill, New York, 1959, pp. 61–89.

[8] D. Morvan, Physical phenomena and length scales governing the behaviour of wildfires: a case for physical modelling, Fire Technol. 47 (2) (2011) 437–460, doi:10.1007/s10694-010-0160-2.

[9] T.L. Clark, L. Radke, J. Coen, D. Middleton, Analysis of small-scale convective dynamics in a crown fire using infrared video camera imagery, J. Appl. Meteorol. 38 (10) (1999) 1401–1420 10.1175/1520-0450(1999)038<1401:AOSSCD>2.0.CO;2.

[10] B.W. Butler, J. Cohen, D.J. Latham, R.D. Schuette, P. Sopko, K.S. Shannon, D. Jimenez, L.S. Bradshaw, Measurements of radiant emissive power and temperatures in crown fires, Can. J. For. Res. 34 (8) (2004) 1577–1587, doi:10.1139/x04-060.

[11] P.M. Fernandes, H.S. Botelho, F.C. Rego, C. Loureiro, Empirical modelling of surface fire behaviour in maritime pine stands, Int. J. Wildland Fire 18 (6) (2009) 698–710, doi:10.1071/WF08023.

[12] E.V. Mueller, Z. Campbell-Lochrie, W.E. Mell, R.M. Hadden, Numerical simulation of low-intensity fire spread in pine litter, in: D.X. Viegas (Ed.), Advances in Forest Fire Research, Imprensa da Universidade de Coimbra, 2018, pp. 1296–1299, doi:10.14195/978-989-26-16-506.

[13] Z. Campbell-Lochrie, C. Walker-Ravena, M. Gallagher, N. Skowronski, E.V. Mueller, R.M. Hadden, Investigation of the role of bulk properties and in-bed structure in the flow regime of buoyancy-dominated flame spread in porous fuel beds, Fire Saf. J. 120 (2021) 103035, doi:10.1016/j.firesaf.2020.103035.

[14] Y. Perez-Ramirez, W.E. Mell, P.A. Santoni, J.B. Tramoni, F. Bosseur, Examination of WFDS in modeling spreading fires in a furniture calorimeter, Fire Technol. 53 (5) (2017) 1795–1832, doi:10.1007/s10694-017-0657-z.

[15] E.V. Mueller, M.R. Gallagher, N. Skowronski, R.M. Hadden, Approaches to modeling bed drag in pine forest litter for wildland fire applications, Transp. Porous Media 138 (3) (2021) 637–660, doi:10.1007/s11242-021-01637-8.

[16] K.L. Clark, W.E. Heilman, N.S. Skowronski, M.R. Gallagher, E. Mueller, R.M. Hadden, A. Simeoni, Fire behavior, fuel consumption, and turbulence and energy exchange during prescribed fires in pitch pine forests, Atmosphere 11 (3) (2020), doi:10.3390/atmos11030242.

[17] A.M. Grishin, Mathematical Modeling of Forest Fires and New Methods of Fighting Them, Publishing House of the Tomsk State University, Tomsk, Russia, 1997.

[18] M. Larini, F. Giroud, B. Porterie, J.-C. Loraud, A multiphase formulation for fire propagation in heterogeneous combustible media, Int. J. Heat Mass Transf. 41 (6) (1998) 881–897, doi:10.1016/S0017-9310(97)00173-7.

[19] B. Porterie, J.L. Consalvi, A. Kaiss, J.C. Loraud, Predicting wildland fire behavior and emissions using a fine-scale physical model, Numer. Heat Transf., Part A 47 (6) (2005) 571–591, doi:10.1080/10407780590891362.

[20] W. Mell, A. Maranghides, R. McDermott, S.L. Manzello, Numerical simulation and experiments of burning douglas fir trees, Combust. Flame 156 (10) (2009) 2023–2041, doi:10.1016/j.combustflame.2009.06.015.

[21] A. Dahale, S. Ferguson, B. Shotorban, S. Mahalingam, Effects of distribution of bulk density and moisture content on shrub fires, Int. J. Wildland Fire 22 (5) (2013) 625, doi:10.1071/WF12040.

[22] M. Kaviany, Principles of Heat Transfer in Porous Media, Springer, 1995.

[23] L. Giani, G. Groppi, E. Tronconi, Heat transfer characterization of metallic foams, Ind. Eng. Chem. Res. 44 (24) (2005) 9078–9085, doi:10.1021/ie050598p.

[24] S. Mancin, C. Zilio, A. Diani, L. Rossetto, Air forced convection through metal foams: experimental results and modeling, Int. J. Heat Mass Transf. 62 (1) (2013) 112–123, doi:10.1016/j.ijheatmasstransfer.2013.02.050.

[25] J.M.C. Mendes-Lopes, J.M.P. Ventura, J.A.M. Rodrigues, Determination of heat transfer coefficient through a matrix of *Pinus pinaster* needles, in: Proceedings of the Fourth International Conference on Forest Fire Research, 2002.

[26] R. Susott, Differential scanning calorimetry of forest fuels, For. Sci. 28 (4) (1982) 839–851, doi:10.1093/forestscience/28.4.839.

[27] M. Statheropoulos, S. Liodakis, N. Tzamtzis, A. Pappa, S. Kyriakou, Thermal degradation of *Pinus halepensis* pine-needles using various analytical methods, J. Anal. Appl. Pyrolysis 43 (2) (1997) 115–123, doi:10.1016/S0165-2370(97)00064-8.

[28] S. Liodakis, D. Bakirtzis, A. Dimitrakopoulos, Ignition characteristics of forest species in relation to thermal analysis data, Thermochim. Acta 390 (1–2) (2002) 83–91, doi:10.1016/S0040-6031(02)00077-1.

[29] D.D. Evans, H.W. Emmons, Combustion of wood charcoal, Fire Saf. J. 1 (1) (1977) 57–66.

[30] V. Tihay, Contribution Expérimentale et Théorique Pour la Modélisation de la Combustion dans les Feux de Forêt, Université de Corse, 2007 Ph.D. thesis.

[31] C.R. Boardman, M.A. Dietenberger, D.R. Weise, Specific heat capacity of wildland foliar fuels to 434 °C, Fuel 292 (2021), doi:10.1016/j.fuel.2021.120396.

[32] M. El Houssami, J.C. Thomas, A. Lamorlette, D. Morvan, M. Chaos, R. Hadden, A. Simeoni, Experimental and numerical studies characterizing the burning dynamics of wildland fuels, Combust. Flame 168 (2016) 113–126, doi:10.1016/j.combustflame.2016.04.004.

[33] Z. Campbell-Lochrie, C. Walker-Rávena, E.V. Mueller, R.M. Hadden, The effect of interstitial flow on the burning dynamics of porous fuel beds, in: D.X. Viegas (Ed.), Advances in Forest Fire Research, Imprensa da Universidade de Coimbra, Coimbra, 2018, pp. 650–660, doi:10.14195/978-989-26-16-506_72.

[34] J. Thomas, Improving the Understand of the Fundamental Mechanism that Influence the Ignition and Burning Dynamics of Porous Wildland Fuels, University of Edinburgh, School of Engineering, Edinburgh, UK, 2016 Ph.D. thesis.

[35] B.N. Taylor, C.E. Kuyatt, Guidelines for evaluating and expressing the uncertainty of NIST measurement results, NIST Technical Note 1297, National Institute of Standards and Technology, Gaithersburg, MD, 1994.

[36] B.T. Barnes, Total radiation from polished and from soot-covered nickel, Phys. Rev. 34 (7) (1929) 1026–1030, doi:10.1103/PhysRev.34.1026.

[37] P.R.N. Childs, J.R. Greenwood, C.A. Long, Review of temperature measurement, Rev. Sci. Instrum. 71 (8) (2000) 2959–2978, doi:10.1063/1.1305516.

[38] M.W. Chase Jr., NIST-JANAF thermochemical tables, J. Phys. Chem. Ref. Data, Monogr. 9 (1998) 59–60.

[39] A. Simeoni, J.C. Thomas, P. Bartoli, P. Borowieck, P. Reszka, F. Colella, P.A. Santoni, J.L. Torero, Flammability studies for wildland and wildlandurban interface fires applied to pine needles and solid polymers, Fire Saf. J. 54 (2012) 203–217, doi:10.1016/j.firesaf.2012.08.005.

[40] K. McGrattan, R. McDermott, S. Hostikka, J. Floyd, M. Vanella, C. Weinschenk, K. Overholt, Fire Dynamics Simulator (Version 6), User's Guide, Technical Report, National Institute of Standards and Technology, Gaithersburg, Maryland, 2021.

[41] O.P. Korobeinichev, S.M. Kumaran, D. Shanmugasundaram, V. Raghavan, S.A. Trubachev, A.A. Paletsky, A.G. Shmakov, R.K. Glaznev, A.A. Chernov, A.G. Tereshchenko, Experimental and numerical study of flame spread over bed of pine needles, Fire Technol. 58 (2021) 1227–1264, doi:10.1007/s10694-021-01190-2.

[42] K. McGrattan, R. McDermott, S. Hostikka, J. Floyd, M. Vanella, C. Weinschenk, K. Overholt, Fire Dynamics Simulator (Version 6), Technical Reference Guide, Technical Report, National Institute of Standards and Technology, Gaithersburg, Maryland, 2021.

[43] A. Žukauskas, Heat transfer from tubes in crossflow, in: Advances in Heat Transfer, vol. 8, Elsevier, 1972, pp. 93–160.

[44] M. El Houssami, A. Lamorlette, D. Morvan, R.M. Hadden, A. Simeoni, Framework for submodel improvement in wildfire modeling, Combust. Flame 190 (2018) 12–24, doi:10.1016/j.combustflame.2017.09.038.

[45] W. Tang, M. Finney, S. McAllister, M. Gollner, An experimental study of intermittent heating frequencies from wind-driven flames, Front. Mech. Eng. 5 (34) (2019) 1–9, doi:10.3389/fmech.2019.00034.

[46] G. Maragkos, T. Beji, Review of convective heat transfer modelling in CFD simulations of fire-driven flows, Appl. Sci. 11 (11:5240) (2021) 1–24, doi:10.3390/app11115240.